Ceramics International

Submitted September 16th, 2015

Revised December 8th, 2015

Effect of composition on lithium-ion conductivity for perovskite-type lithium-strontium-tantalum-zirconium-oxide solid electrolytes

Keisuke Kimura, Kota Wagatsuma, Tomohiro Tojo, Ryoji Inada*, and Yoji Sakurai

Department of Electrical and Electronic Information Engineering, Toyohashi University of Technology, 1-1 Hibarigaoka, Tempaku-cho, Toyohashi, Aichi 441-8580, Japan.

*Corresponding author

Ryoji Inada, Associate Professor

Postal address: Toyohashi University of Technology, 1-1 Tempaku-cho, Toyohashi, Aichi 441-8580, Japan

Phone: +81-532-44-6723

Fax: +81-532-44-6757

E-mail address: inada@ee.tut.ac.jp

Abstract

We synthesized $Li_{2x-y}Sr_{1-x}Ta_yZr_{1-y}O_3$ (LSTZ, x = 0.75y) with various Ta contents y = 0.60, 0.70, 0.75, 0.77 and 0.8 via a conventional solid state reaction method and investigated their crystal phase, microstructure and lithium-ion conductivity. Almost single phase perovskite-type structured LSTZ was obtained at y = 0.60–0.75 and their lattice sizes were increased with increasing y, indicating that Sr^{2+} and Zr^{4+} are successfully substituted by Li^+ and Ta^{5+} with smaller ionic radii in these three samples. On the other hand, LSTZ with higher Ta contents y = 0.77 and 0.8 included some impurity phases such as $LiTaO_3$, $SrTa_2O_6$ and $Sr_2Ta_2O_7$. A solid solution range for Ta into Zr site for LSTZ is expected to be $y \leq 0.75$. Both the bulk and total (bulk + grain-boundary) ionic conductivity of LSTZ monotonically increased with y from 0.60 to 0.75. Maximum bulk and total (bulk + grain-boundary) conductivities of 2.8×10^{-4} Scm^{-1} and 2.0×10^{-4} Scm^{-1} at 27°C were obtained in LSTZ with y = 0.75.

Keywords: perovskite; oxide; solid electrolyte; lithium ion conductivity; rechargeable battery

1. Introduction

All-solid-state lithium-ion batteries (LiBs) are expected to be one of the next generation of energy storage devices because of their high energy density, high safety and excellent cycle stability [1–3]. The development of solid inorganic lithium-ion conducting materials for use as a solid electrolyte is the most important issue in order to realize solid-state batteries. The materials used for solid electrolyte must have not only high lithium-ion conductivity $\sigma > 10^{-3}$ Scm^{-1} at room temperature but also chemical stability against metallic lithium or lithiated negative electrode, air and moisture. Although oxide based solid electrolyte materials have rather lower σ than sulfide based ones, they have other advantages such as their chemical stability and ease of handling. Among the oxide-based lithium-ion conducting solid electrolyte materials, perovskite-type $Li_{0.35}La_{0.55}TiO_3$ (LLT) exhibits very high bulk ionic conductivity above 10^{-3} Scm^{-1} at room temperature [4–10]. However, its grain-boundary conductivity around room temperature is limited only in the order of 10^{-5}–10^{-4} Scm^{-1} [4–8], which leads to much lower total (bulk + grain-boundary) conductivity than for a bulk one. Furthermore, its electronic conductivity can be increased substantially because the Ti^{4+} included in LLT is easily reduced to Ti^{3+} when LLT is in contact with metallic lithium or lithiated graphite inside a battery. It has been reported that the reduction from Ti^{4+} to Ti^{3+} in LLT is caused at the potential of 1.6–1.8 V vs. Li/Li^+ [9, 10]. Such electrochemical instability creates significant difficulty to use this material for the production of solid-state batteries.

Several papers for other perovskite-type lithium-ion conducting oxides with higher stability than LLT have been reported [11–15]. Thangadurai et al. studied lithium-ion conductors $LiSr_{1.65}B_{1.3}B'_{1.7}O_9$ (B = Ti, Zr; B'= Nb, Ta) [11]. Although the Ti-contained materials have a similar stability problem as seen in LLT, they concluded that

$LiSr_{1.65}Zr_{1.3}Ta_{1.7}O_9$ is a lithium-conductor with much higher electrochemical stability than LLT. Although they did not show bulk and grain-boundary conductivity quantitatively, the total (bulk + grain-boundary) conductivity of $LiSr_{1.65}Zr_{1.3}Ta_{1.7}O_9$ was limited to 1.6×10^{-5} Scm^{-1} at 30°C. Watanabe et al. reported the properties of Ta containing $Li_{2x}Sr_{1-2x}M_{0.5-x}Ta_{0.5+x}O_3$ (M = Cr, Fe, Co, Al, Ga, In and Y) [12]. The bulk conductivity attained to 1×10^{-4} Scm^{-1} at 25°C when M = Fe and x = 0.25, but total conductivity is two orders lower than the bulk one due to poor sinterability. Phraewphiphat et al. recently reported a systematical study for crystal structure and conductivity for $Li_xSr_{1-x}M_{(1-x)/2}Ta_{(1+x)/2}O_3$ (M = Al, Ga) [13]. They concluded that higher conductivity was observed in Ga substituted compounds and optimized composition to obtain the highest conductivity is $Li_{0.25}Sr_{0.625}Ga_{0.25}Ta_{0.75}O_3$, but total conductivity around room temperature was limited at around 10^{-5} Scm^{-1}.

Chen et al. investigated the crystal phase and ionic conductivity in $Li_{2x-y}Sr_{1-x}Ta_yZr_{1-y}O_3$ (LSTZ, x = 0.75y) with four different Ta contents y = 0.25, 0.5, 0.75 and 1 [14]. They reported that the perovskite structure can be obtained at Ta contents y = 0.25, 0.5 and 0.75, and the highest bulk and total conductivity of 2.0×10^{-4} Scm^{-1} and 0.8×10^{-4} Scm^{-1} at 30°C is achieved in LSTZ with y = 0.75. Although this total conductivity is lower than densified LLT as reported in [8], LSTZ is found to be stable, at least above 1 V vs Li/Li^+ and has a wider electrochemical potential window than LLT [14], so that several negative electrode materials operating at high potential for lithium-ion storage such as $Li_4Ti_5O_{12}$, TiO_2 and Nb_2O_5 can be potentially used for constituting solid-state batteries with a LSTZ solid electrolyte.

It should be noted that Chen et al. have not shown the properties for LSTZ with Ta content y near 0.75 in detail [14], so that it has not yet been clarified that a further increase

of y is possible to obtain a pure perovskite-type structure and LSTZ with y = 0.75 ($Li_{3/8}Sr_{7/16}Ta_{3/4}Zr_{1/4}O_3$) and if this is an optimized composition to achieve the highest conductivity or not. In this paper, we synthesized LSTZ with different Ta contents y = 0.60, 0.70, 0.75, 0.77 and 0.8 via conventional solid state reaction method and investigated their crystal phase, microstructure and lithium-ion conducting property systematically. Based on experimental results, the optimized composition of LSTZ for high ionic conductivity is discussed.

2. Experimental

LSTZ with different Ta contents y = 0.6, 0.7, 0.75, 0.77 and 0.8 was synthesized via a conventional solid state reaction method. The detailed nominal composition of five LSTZ samples are summarized in Table 1. LSTZ includes some amounts of vacancy in A-site for perovskite structure depending on y. The contents of Li (2x−y) and vacancy □ (y−x) are increased while those of Sr (1−x) and Zr (1−y) are decreased with increasing y. Stoichiometric amounts of Li_2CO_3 (Kojundo Chemical Laboratory Co., Ltd., 99.99%), $SrCO_3$ (Kojundo Chemical Laboratory Co., Ltd., 99.9%), ZrO_2 (Kojundo Chemical Laboratory Co., Ltd., 98%) and Ta_2O_5 (Kojundo Chemical Laboratory Co., Ltd., 99.9%) were ground and mixed with ethanol for 5 h by planetary ball-milling (Nagao System, Planet M2-3F) with zirconia balls, and then calcined at 1100°C for 12 h in air using an alumina crucible. The calcined powders were ground again, and then pressed into pellets at a pressure of 300 MPa by cold isostatic pressing (CIP). Finally, the LSTZ pellets were sintered at 1300°C for 15 h in air using an alumina crucible.

The identification of the crystal phase of LSTZ samples with different compositions was evaluated by X-ray diffraction (XRD, Rigaku Multiflex, RIGAKU) using CuKα

radiation (λ = 0.15418 nm), with a measurement angle range of 2θ = 5–90° and a step interval of 0.01°. Using the X-ray diffraction (XRD) data for LSTZ samples, lattice parameters were calculated by Rigaku PDXL XRD analysis software. A scanning electron microscope (SEM, VE-8800, KEYENCE) was used to observe the surface microstructure of each sintered LSTZ. Energy dispersive X-ray (EDX) analysis was performed using a field-emission scanning electron microscope (FE-SEM, SU8000 Type II, Hitachi) to investigate the distribution of Sr, Ta, Zr and Al (contaminated from the crucible during high temperature sintering) elements in sintered LSTZ. The elementary composition in each sample was measured by inductively coupled plasma optical emission spectroscopy (ICP-OES). Ionic conductivity was evaluated at a temperature range from 27 to 150°C by an AC impedance measurement with a frequency from 5 Hz to 5 MHz with an applied voltage amplitude of 0.1 V, using both Hioki Chemical Impedance Meter 3532-80 (for the measurement up to 1 MHz) and Hioki LCR Hightester 3532-50 (for the measurement from 1 MHz to 5 MHz). Before the conductivity measurements, both parallel surfaces of the sintered LSTZ pellet were sputtered with lithium-ion blocking Au electrodes.

3. Results and discussion

The color of all sintered LSTZ samples with different Ta contents y were white and the diameter and thickness were 10 mm and 2 mm, respectively. XRD patterns of LSTZ samples with different compositions are shown in Fig. 1. The main diffraction peaks for LSTZ-1 with y = 0.60, LSTZ-2 with y = 0.70 and LSTZ-3 with y = 0.75 belong to the cubic perovskite structure with a space group *Pm*-3*m*. On the other hand, LSTZ-4 with y = 0.77 and LSTZ with y = 0.8 include impurity phases such as $LiTaO_3$, $SrTa_2O_6$ and $Sr_2Ta_2O_7$ together with the peaks from the cubic perovskite phase, indicating that these

compositions are difficult to obtain single phase perovskite-type composites without forming any impurity phases. The peak intensity from impurity phases for LSTZ-5 with y = 0.80 is larger than that for LSTZ with y = 0.77. It is noted that we applied an additional heat treatment at 1300°C for 15 h to LSTZ-4 and LSTZ-5, but no notable change was confirmed in the XRD data and the impurity phases as mentioned above could not be avoided.

Enlarged diffraction peaks for (110) plane for all LSTZ samples are shown in Fig. 2. As can be seen, the diffraction peaks shifted toward a higher angle with increasing Ta contents y from 0.6 to 0.75. It should be noted that such peak shifts depending on y are confirmed in other diffraction peaks, indicating that the lattice sizes of LSTZ decreases with increasing y. The ionic radii of Sr^{2+} (132 pm) and Zr^{4+} (72 pm) are larger than the substitution elements Li^{+} (90 pm) and Ta^{5+} (64 pm), so that it is expected that Sr^{2+} and Zr^{4+} are successfully substituted by Li^{+} and Ta^{5+} with smaller ionic radii in these three LSTZ samples. From the XRD data, the lattice parameters *a* of these three LSTZ samples with pure cubic perovskite structure are estimated to be 4.012 Å for LSTZ-1 with y = 0.60, 3.998 Å for LSTZ-2 with y = 0.7 and 3.992 Å for LSTZ-3 with y = 0.75. On the other hand, the peaks for LSTZ-4 and LSTZ-5 with y = 0.77 and 0.80 are shifted slightly toward a lower angle compared with LSTZ with y = 0.75. Although the compositions of perovskite phase included in LSTZ-4 and LSTZ-5 samples are slightly different with LSTZ-3, a solid solution range for Ta into Zr site for LSTZ is expected to be $y \leq 0.75$.

Fig. 3 shows the microstructure of the surface for all LSTZ samples observed by SEM. As can be seen, LSTZ-1, LSTZ-2 and LSTZ-3 without including any impurity phases, have a well densified structure with LSTZ grains with the size of 5–10 μm and pores are not observed. As shown in Fig. 1(b) and (d), both LSTZ-4 and LSTZ-5 include

$LiTaO_3$, $SrTa_2O_6$ and $Sr_2Ta_2O_7$ as impurity phases, but the grain sizes of LSTZ-5 are much smaller than those of LSTZ-4 and some pores are clearly confirmed. This is consistent with the data for measured densities in Table 2. Compared with LSTZ-4, LSTZ-5 includes a larger quantity of impurity phases, which inhibits the sintering process and grain growth of LSTZ. The SEM image and corresponding elementary mapping of Sr, Ta and Zr of LSTZ-3 are also shown in Fig. 4(a-d). It can be seen that the distributions of Sr, Ta and Zr are nearly identical. In EDX spectrum shown in Fig. 4(e), the EDX spectrum from Al cannot be confirmed clearly, suggesting that Al contamination from the alumina crucible during high temperature sintering are negligible.

The elementary compositions evaluated by an ICP-OES analysis for LSTZ-1, LSTZ-2 and LSTZ-3 are summarized in Table 2, together with the densities of all samples. The compositions of LSTZ-4 and LSTZ-5 are not evaluated because they include many impurity phases (see Fig. 1). The density of each sintered LSTZ was determined from the weight and physical dimensions. As can be seen, the densities of LSTZ tend to be increased with Ta contents y from 0.6 to 0.75, due to both the increase of the level for heavier Ta substitution and the reduced lattice sizes with y as mentioned above. It is worth noting that our LSTZ-3 with y = 0.75 has higher density of 6.23 gcm^{-3} than a sample with the same composition (= 5.95 gcm^{-3}) reported in the literature [14]. Previously reported LSTZ with y = 0.75 also includes small amount of $LiTaO_3$ as impurity phases. On the other hand, LSTZ-4 and LSTZ-5 with a larger y = 0.77 and 0.80 and impurity phases have lower densities than LSTZ-3. The obtained molar ratios of Sr, Ta and Zr in LSTZ-1, LSTZ-2 and LSTZ-3 are nearly corresponding to nominal compositions, but small amount of Li deficiency was observed in these three samples. Li loss of LSTZ could be caused during the high temperature sintering process and leads to form impurity phases

such as $SrTa_2O_6$ and $Sr_2Ta_2O_7$ [14], but these impurity phases are difficult to detect in XRD measurements for LSTZ-1, LSTZ-2 and LSTZ-3 (see Fig. 1).

The conductivity of LSTZ-1, LSTZ-2 and LSTZ-3 without impurity phases was examined by AC impedance spectroscopy using Au electrodes. Fig. 5 shows typical impedance plots measured at 27°C. Since the geometrical parameters of all LSTZ samples are identical, both the real and the imaginary parts of impedance Z and Z" can be compared directly. For all LSTZ samples, semicircle(s) and linear portion data were obtained in high and low frequency regions, indicating that the conducting nature is primarily ionic. The intercept point of the linear tail in the low frequency range with a real axis nearly corresponds to total (bulk + grain-boundary) resistance R_{total}. As can be seen, these plots can be resolved into bulk R_b and grain-boundary resistances R_{gb}. The ratios of R_b to R_{total} for these three LSTZ samples are ranged from 0.64 to 0.77 and the contribution of R_{gb} in R_{total} is not so large, which is quite different from perovskite-type LLT [4–10]. LSTZ-3 with y = 0.75 has the lowest R_b and R_{total}, indicating that this sample has the best ionic conducting properties.

Bulk, grain-boundary and total conductivities σ_b, σ_{gb} and σ_{total} for each LSTZ sample can be calculated by $L(R_bA)^{-1}$, $L(R_{gb}A)^{-1}$ and $L(R_{total}A)^{-1}$, respectively. Here, L and A are the thickness and surface area of the pellet sample. The values of σ_b, σ_{gb} and σ_{total} at 27°C for all LSTZ samples calculated from the data in Fig. 5 are summarized in Table 3 and Fig. 6. It is evident that σ_b, σ_{gb} and σ_{total} are monotonically increased with increasing the Ta contents y from 0.60 to 0.75. Moreover, σ_{gb} is significantly higher than σ_b so that σ_{total} is close to σ_b for all LSTZ samples. As mentioned above, the lattice parameters of LSTZ are decreased with increasing y and the Li concentration. The decrease of lattice size generally result into the reduction of bottle-neck size for Li^+ migration in LSTZ.

Therefore, is we believe that σ_b of LSTZ is optimized by tuning Li–Li site distance depending on the Li concentration. Maximum $\sigma_b = 2.8 \times 10^{-4}$ Scm^{-1} and $\sigma_{total} = 2.0 \times 10^{-4}$ Scm^{-1} at 27°C are obtained in LSTZ-3 with y = 0.75. These properties are much superior to LSTZ with the same compositions reported in the literature [14]. Particularly, σ_{total} of our LSTZ-3 is approximately 2.5 times higher than the reported one (= 0.8×10^{-4} Scm^{-1} at 30°C). This is mainly attributed to both the avoidance of the impurity phases and a larger density in our sample (= 6.23 gcm^{-3}) than previously reported one (= 5.95 gcm^{-3}). σ_{total} in LSTZ-3 is comparable with garnet-type $Li_7La_3Zr_2O_{12}$ (LLZ) sintered with mother powder [15–20], but in this work, we did not use mother powder for sintering LSTZ. Moreover, it should be noted that LSTZ-1 and LSTZ-2 with y = 0.6 and 0.7 have higher σ_b than LSTZ with y = 0.5 ($\sigma_b = 3.34 \times 10^{-7}$ Scm^{-1} at 30°C) reported in [14], suggesting that higher lithium-ion concentrations in perovskite-type LSTZ are effective to achieve high conductivity.

The temperature dependence of total conductivity σ_{total} for LSTZ-1, LSTZ-2 and LSTZ-3 was also measured in the temperature range from 27 to 150°C. Fig. 7 shows the Arrhenius plots for three LSTZ samples as a function of inverse of temperature T^{-1}. The temperature dependence of σ_{total} for each LSTZ sample is well expressed by the Arrhenius equation $\sigma_{total}T = \sigma_0 \exp\left(-E_a\left(k_BT\right)^{-1}\right)$, where σ_0 is constant, E_a is the activation energy of conductivity and k_B is the Boltzmann constant (= 1.381×10^{-23} J/K). E_a for σ_{total} of each sample can be estimated from the slope of $\sigma_{total}T$ data plotted in Fig. 7. Estimated E_a for each LSTZ sample are listed in Table 3 together with σ_{bulk} and σ_{total} at 27°C. As can be seen, E_a of LSTZ samples are decreased monotonically with increasing y from 0.60 to 0.75. LSTZ-3 with both the highest σ_{bulk} and σ_{total} shows the lowest E_a = 0.37 eV among

the samples. Temperature dependence of σ_{total} for LSTZ-3 is also shown in Fig. 8, together with AC impedance plots at different temperatures as an inset. It is confirmed that the σ_{total} of LSTZ-3 enhances above 10^{-3} S cm^{-1} at temperature above 70°C and attains to 1.2 $\times$ 10^{-2} S cm^{-1} at 150°C.

4. Conclusion

Perovskite-type $Li_{2x-y}Sr_{1-x}Ta_yZr_{1-y}O_3$ (LSTZ, x = 0.75y) solid electrolytes with different Ta contents y = 0.6–0.8 were prepared via a conventional solid state reaction method and their crystal phases, microstructures and lithium-ion conducting properties were investigated. A single phase perovskite-type structure was obtained in LSTZ sample with y = 0.6–0.75 and the lattice sizes of LSTZ were increased with y. However, the LSTZ samples with y above 0.77 contained impurity phases such as $LiTaO_3$, $SrTa_2O_6$ and $Sr_2Ta_2O_7$, indicating that a solid solution range for Ta into Zr site for perovskite-type LSTZ is expected to be $y \leq 0.75$. Both bulk and total (bulk + grain-boundary) ionic conductivity of LSTZ monotonically increased with y from 0.6 to 0.75. Maximum bulk and total conductivities of 2.8 $\times$ 10^{-4} Scm^{-1} and 2.0 $\times$ 10^{-4} Scm^{-1} at 27°C was obtained in LSTZ with y = 0.75. This conductivity is attractive for the application to oxide-based all-solid-state lithium-ion batteries.

Acknowledgments

This work was partly supported by JSPS KAKENHI (Challenging Exploratory Research) Grant Number 26630111 from the Japan Society for the Promotion of Science (JSPS) and Research Foundation for the Electrotechnology of Chubu (R-25209).

References

[1] K. Takada, Progress and prospective of solid-state lithium batteries, Acta Mater. 61 (2013) 759–770.

[2] M. Tatsumisago, M. Nagao, A. Hayashi, Recent development of sulfide solid electrolytes and interfacial modification for all-solid-state rechargeable lithium batteries, J. Asian Ceram. Soc. 1 (2013) 17–25.

[3] S. Teng, J. Tan, A. Tiwari, Recent developments in garnet based solid state electrolytes for thin film batteries, Current Opinion in Solid State and Materials Science 18 (2014) 29–38.

[4] Y. Inaguma, C. Liquan, M. Itoh, T. Nakamura, High ionic conductivity in lithium lanthanum titanate, Solid State Commun. 86 (1993) 689–693.

[5] Y. Harada, H. Watanabe, J. Kuwano, Y. Saito, Lithium ion conductivity of A-site deficient perovskite solid solutions, J. Power Sources. 81–82 (1999) 777–781.

[6] C.W. Ban, G.M. Choi, The effect of sintering on the grain boundary conductivity of lithium lanthanum titanates, Solid State Ionics 140 (2001). 285–292.

[7] J. Wolfenstine, J.L. Allen, J. Read, J. Sakamoto, G. Gonalez-Doncel, Hot-pressed $Li_{0.33}La_{0.57}TiO_3$, J. Power Sources 195 (2010) 4124–4128.

[8] Y. Inaguma, M Nakashima, A rechargeable lithium-air battery using a lithium ion-conducting lanthanum lithium titanate ceramics as an electrolyte separator, J. Power Sources 228 (2013) 250–255.

[9] C.H. Chen, K. Amine, Ionic conductivity, lithium insertion and extraction of lanthanum lithium titanate, Solid State Ionics 144 (2001) 51–57.

[10] C. Hua, X. Fang, Z. Wang, L. Chen, Lithium storage in perovskite lithium lanthanum titanate, Electrochem. Commun. 32 (2013) 5–8.

[11] V. Thangadurai, A.K. Shukla, J. Gopalakrishnan, $Li_{1.65}Sr_{0.35}B_{1.3}B'_{1.7}O_9$ (B = Ti, Zr; B' = Nb, Ta): New Lithium Ion Conductors Based on the Perovskite Structure, Chem. Mater. 11 (1999) 835–839.

[12] H. Watanabe, J. Kuwano, Formation of perovskite solid solutions and lithium-ion conductivity in the compositions, $Li_{2x}Sr_{1-2x}M^{III}_{0.5-x}Ta_{0.5+x}O_3$ (M = Cr, Fe, Co, Al, Ga, In, Y), J. Power Sources 68 (1997) 421–426.

[13] T. Phraewphiphat, M. Iqbal, K. Suzuki, Y. Matsuda, M. Yonemura, M. Hirayama, R. Kanno, Syntheses, structures, and ionic conductivities of perovskite-structured lithium–strontium–aluminum/gallium–tantalum-oxides, J. Solid State Chem. 225 (2015) 431–437.

[14] C.H. Chen, S. Xie, E. Sperling, A.S. Yang, G. Henriksen, K. Amine, Stable lithium-ion conducting perovskite lithium–strontium–tantalum–zirconium–oxide system, Solid State Ionics 167 (2004) 263–272.

[15] R. Murugan, V. Thangadurai, W. Weppner, Fast lithium ion conduction in garnet-type $Li_7La_3Zr_2O_{12}$, Angew. Chem. Int. Ed. 46 (2007) 7778–7781.Angew. Chem. Int. Ed. 46 (2007) 7778–7781.

[16] S. Kumazaki, Y. Iriyama, K.H. Kim, R. Murugan, K. Tanabe, K. Yamamoto, T. Hirayama, Z. Ogumi, High lithium ion conductive $Li_7La_3Zr_2O_{12}$ by inclusion of both Al and Si, Electrochem. Commun. 13 (2011) 509–512.

[17] R. Murugan, S. Ramakumar, N. Janani, High conductive yttrium doped $Li_7La_3Zr_2O_{12}$ cubic lithium garnet, Electrochem. Commun. 13 (2011) 1373–1375.

[18] Y. Shimonishi, A. Toda, T. Zhang, A. Hirano, N. Imanishi, O. Yamamoto, Y. Takeda, Synthesis of garnet-type $Li_{7-x}La_3Zr_2O_{12-1/2x}$ and its stability in aqueous solutions, Solid State Ionics 183 (2011) 48–53.

[19] Y. Li, J. Han, C. Wang, H. Xie, J.B. Goodenough, Optimizing Li^+ conductivity in a garnet framework, J. Mater. Chem. 22 (2012) 15357–15361.

[20] R. Inada, K. Kusakabe, T. Tanaka, S. Kudo, Y. Sakurai, Synthesis and properties of Al-free $Li_{7-x}La_3Zr_{2-x}Ta_xO_{12}$ garnet related oxides, Solid State Ionics 262 (2014) 568–572.

[21] V. Thangadurai, D. Pinzaru, S. Narayanan, A.K. Baral, Fast solid-state Li ion conducting garnet-type structure metal oxides for energy storage, J. Phys. Chem. Lett. 6 (2015) 292–299.

[22] X. Tong, V. Thangadurai, E.D. Wachsman, Highly conductive Li garnets by a multielement doping strategy, Inorg. Chem. 54 (2015) 3600–3607.

Table 1. Nominal composition of $Li_{2x-y}Sr_{1-x}Ta_yZr_{1-y}O_3$ (LSTZ, x = 0.75y) prepared in this study. Symbol □ represents the expected content of A-site vacancy.

Sample name	Li	Sr	□	Ta	Zr
LSTZ-1	0.30	0.55	0.15	0.60	0.40
LSTZ-2	0.35	0.475	0.175	0.70	0.30
LSTZ-3	0.375	0.4375	0.1875	0.75	0.25
LSTZ-4	0.385	0.4225	0.1925	0.77	0.23
LSTZ-5	0.40	0.40	0.20	0.80	0.20

Table 2. Measured densities and elementary compositions of sintered LSTZ samples estimated from ICP-OES analysis. The compositions of LSTZ-4 and LSTZ-5 are not evaluated because they include impurity phases (see Fig. 1). Note that Ta contents for each LSTZ is fixed for the nominal composition (listed in Table 1) to calculate the contents for Li, Sr and Zr.

Sample name	Density / g cm^{-3}	Li	Sr	Ta	Zr
LSTZ-1	6.02	0.225	0.510	0.60	0.371
LSTZ-2	6.20	0.308	0.441	0.70	0.280
LSTZ-3	6.23	0.362	0.412	0.75	0.232
LSTZ-4	6.12	–	–	–	–
LSTZ-5	6.08	–	–	–	–

Table 3. Summary of bulk conductivity σ_b, grain-boundary conductivity σ_{gb}, total conductivity σ_{total}, R_{gb} / R_{total} at 27°C and activation energy E_a for σ_{total} for LSTZ-1 (y = 0.60), LSTZ-2 (y = 0.70) and LSTZ-3 (y = 0.75).

Sample name	σ_b / S cm^{-1} at 27°C	σ_{gb} / S cm^{-1} at 27°C	σ_{total} / S cm^{-1} at 27°C	R_b / R_{total} at 27°C	E_a / eV
LSTZ-1	0.77×10^{-5}	2.7×10^{-5}	0.60×10^{-5}	0.77	0.46
LSTZ-2	1.2×10^{-4}	1.9×10^{-4}	7.3×10^{-5}	0.64	0.39
LSTZ-3	2.8×10^{-4}	7.0×10^{-4}	2.0×10^{-4}	0.69	0.37

Figure captions

Fig. 1. X-ray diffraction patterns of LSTZ samples with different Ta contents y as shown in Table 1: (a) LSTZ-1 (y = 0.60), (b) LSTZ-2 (y = 0.70), (c) LSTZ-3 (y = 0.75), (d) LSTZ-4 (y = 0.77) and (e) LSTZ-5 (y = 0.80).

Fig. 2. Enlarged (110) diffraction peaks for LSTZ samples with different Ta contents y: (a) LSTZ-1 (y = 0.60), (b) LSTZ-2 (y = 0.70), (c) LSTZ-3 (y = 0.75), (d) LSTZ-4 (y = 0.77) and (e) LSTZ-5 (y = 0.80).

Fig. 3. SEM images for sintered LSTZ samples with different Ta contents y: (a) LSTZ-1 (y = 0.60), (b) LSTZ-2 (y = 0.70), (c) LSTZ-3 (y = 0.75), (d) LSTZ-4 (y = 0.77) and (e) LSTZ-5 (y = 0.80).

Fig. 4. (a) SEM image for the surface of LSTZ-3 (y = 0.75) and corresponding elementary mapping of (b) Sr, (c) Ta and (d) Zr obtained from EDX analysis. The EDX spectrum is also shown in (e).

Fig. 5. AC impedance plot obtained at 27°C for sintered LSTZ samples with Ta contents: (a) LSTZ-1 (y = 0.60), (b) LSTZ-2 (y = 0.70) and (c) LSTZ-3 (y = 0.75).

Fig. 6. Bulk conductivity σ_b, grain-boundary conductivity σ_{gb} and total conductivity σ_{total} for sintered LSTZ samples plotted against Ta contents y.

Fig. 7. Arrhenius plots for total conductivity σ_{total} of LSTZ-1 (y = 0.60), LSTZ-2 (y = 0.70) and LSTZ-3 (y = 0.75).

Fig. 8. Total conductivity σ_{total} for LSTZ-3 (y = 0.75) plotted against the inverse of measurement temperature *T*. Inset is the AC impedance plots of this sample measured at 27−150°C.

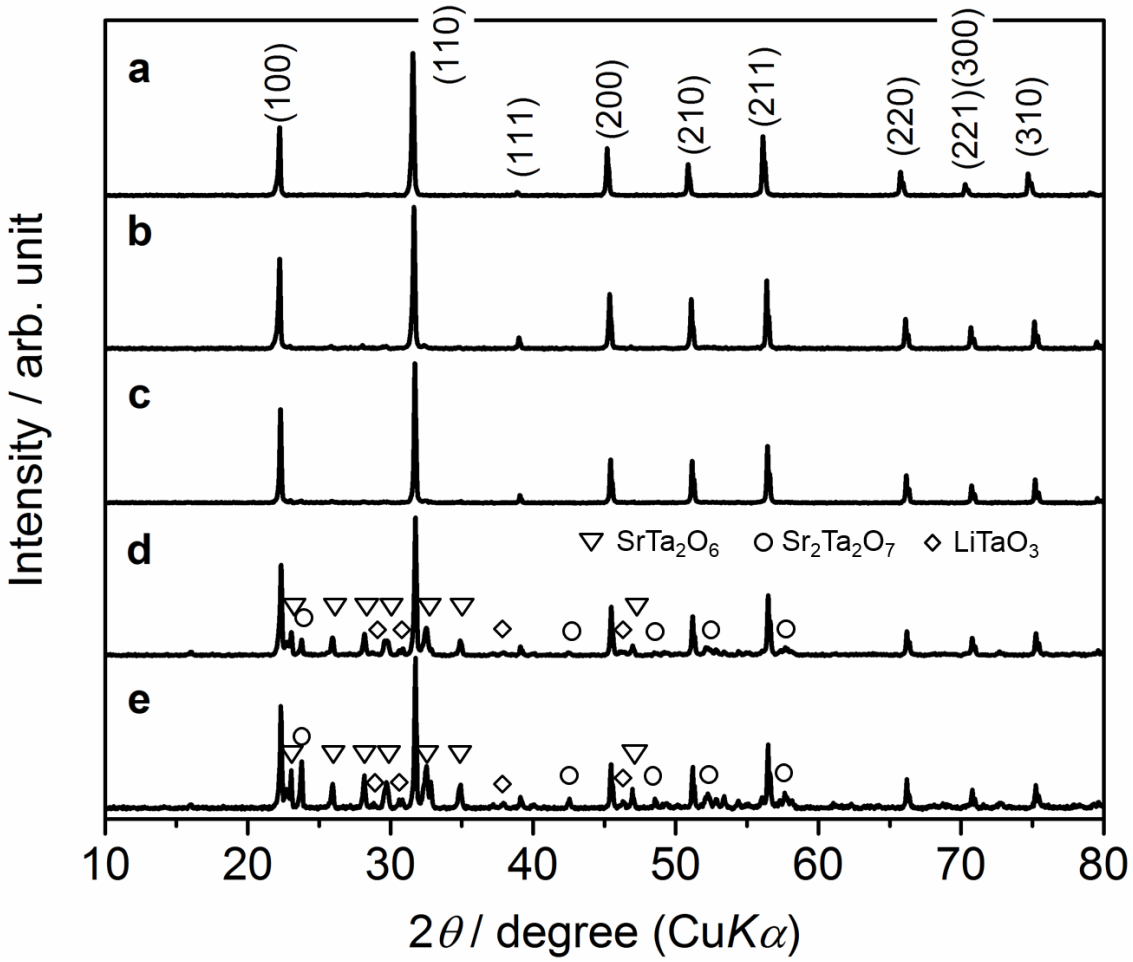
a
b
c
d
e
(100)
(110)
(111)
(200)
(210)
(211)
(220)
(221)(300)
(310)
SrTa2O6
Sr2Ta2O7
LiTaO3
Intensity / arb. unit
10
20
30
40
50
60
70
80
2θ / degree (CuKα)

Fig. 1

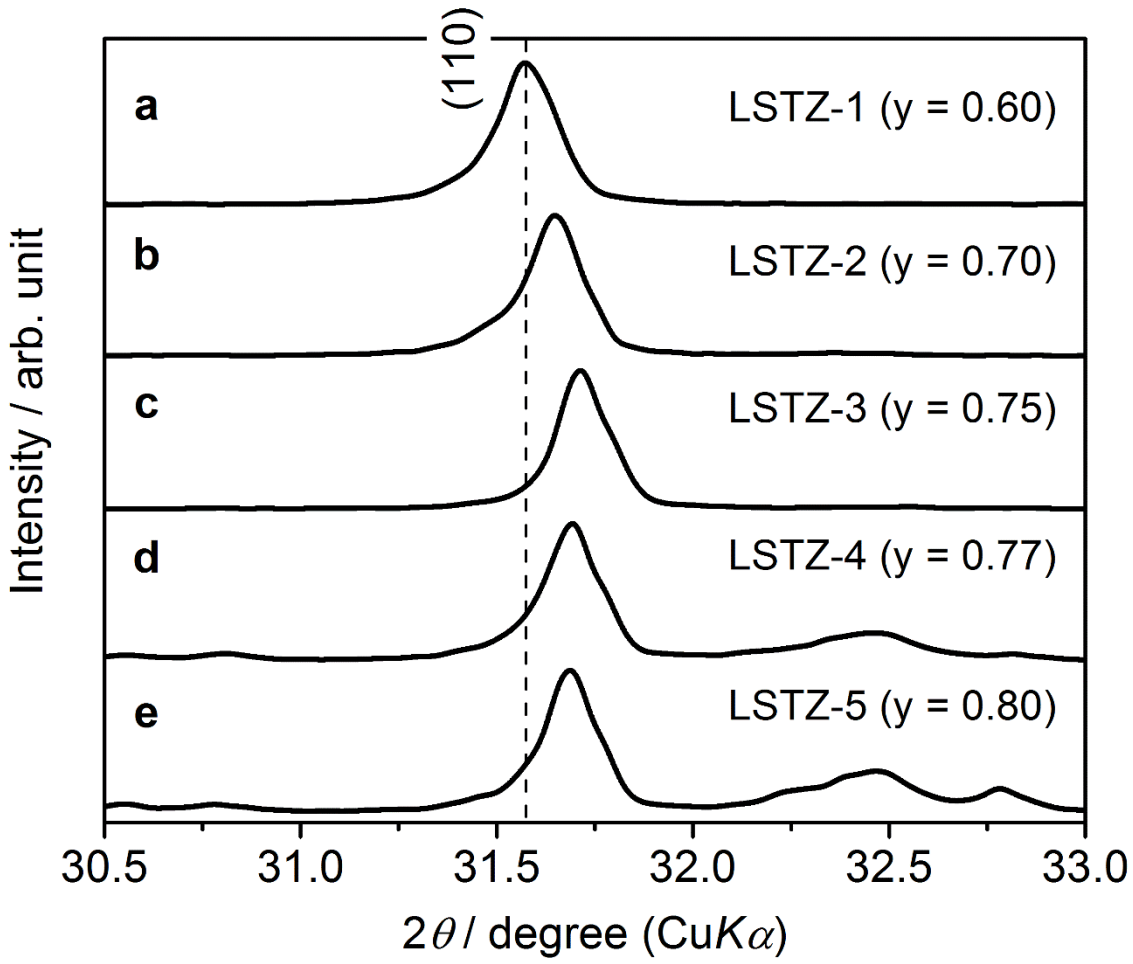
(110)
a
LSTZ-1 (y = 0.60)
b
LSTZ-2 (y = 0.70)
c
LSTZ-3 (y = 0.75)
d
LSTZ-4 (y = 0.77)
e
LSTZ-5 (y = 0.80)
Intensity / arb. unit
30.5
31.0
31.5
32.0
32.5
33.0
2θ / degree (CuKα)

Fig. 2

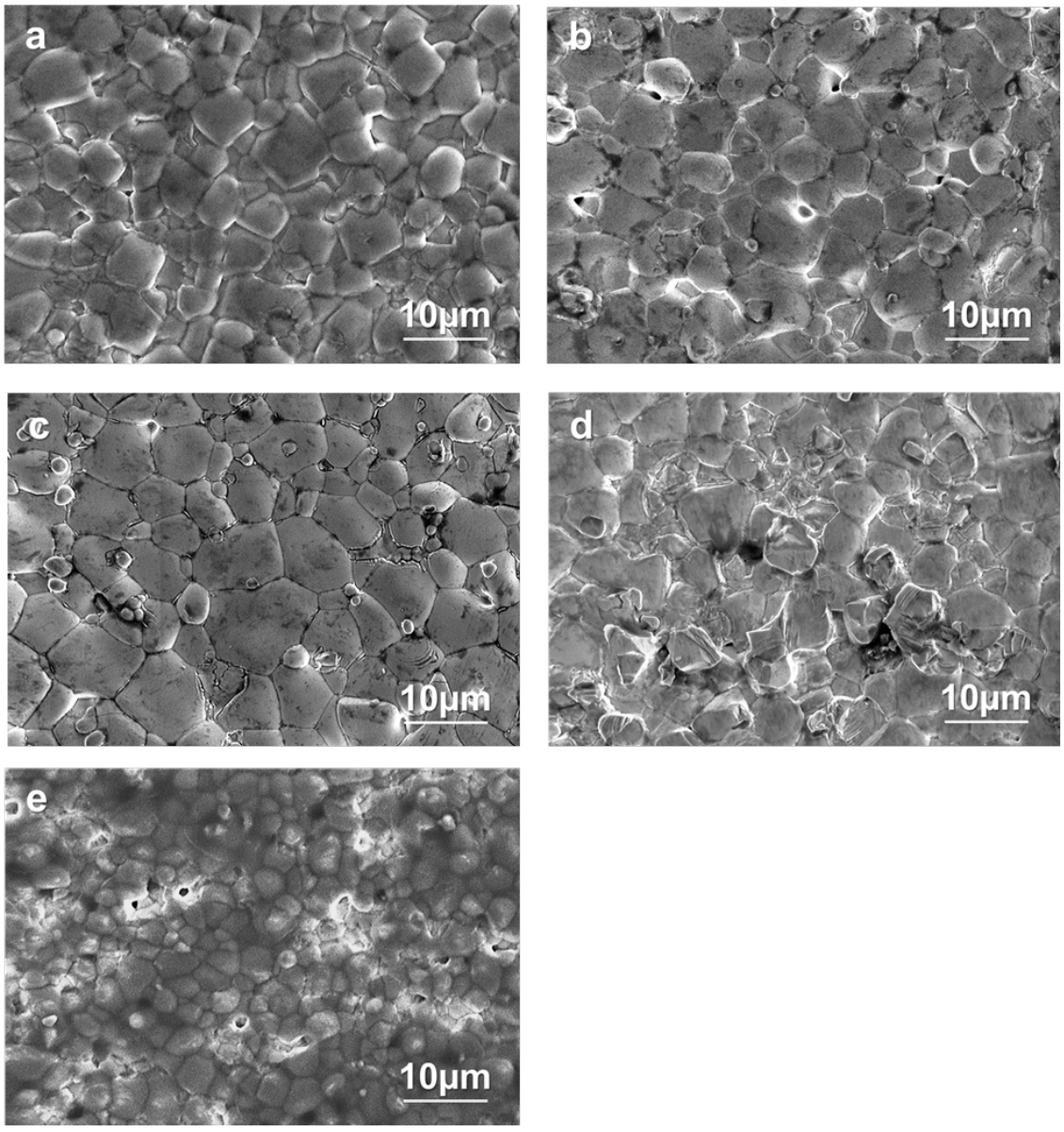

Fig. 3

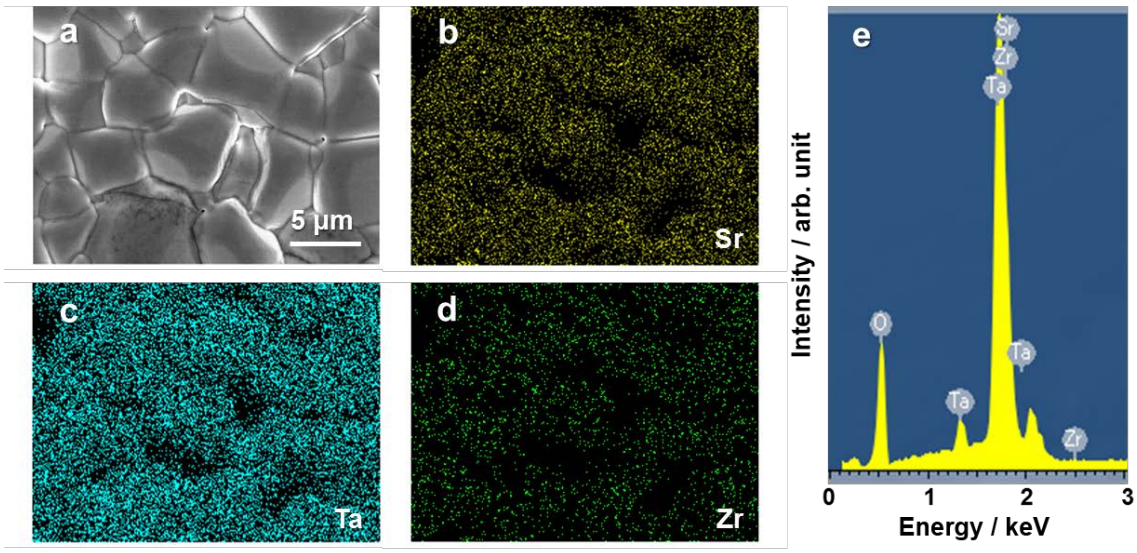
a
5 µm
b
Sr
c
Ta
d
Zr
e
Sr
Zr
Ta
O
Ta
Ta
Zr
Intensity / arb. unit
0
1
2
3
Energy / keV

Fig. 4

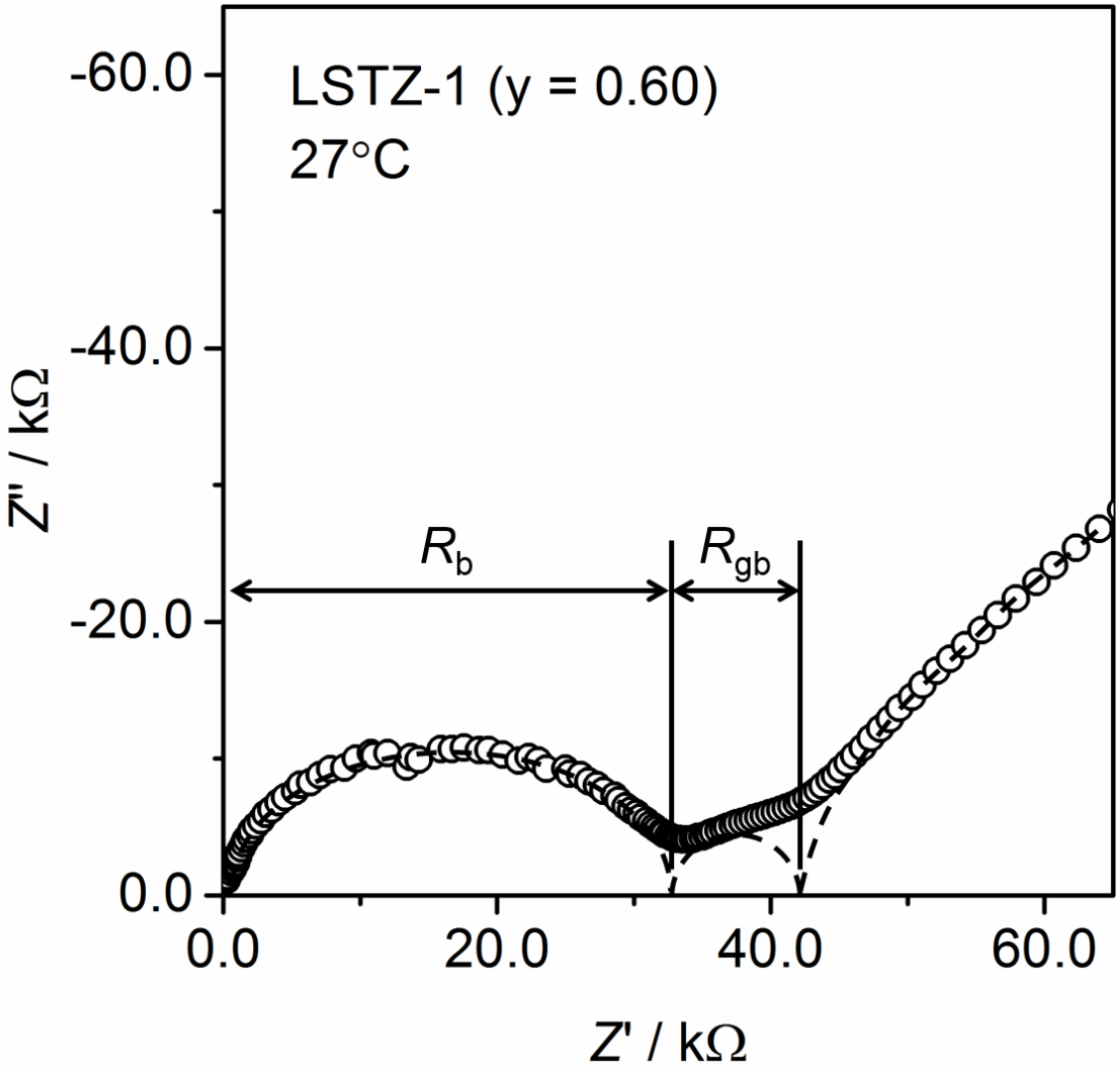

Fig. 5(a)

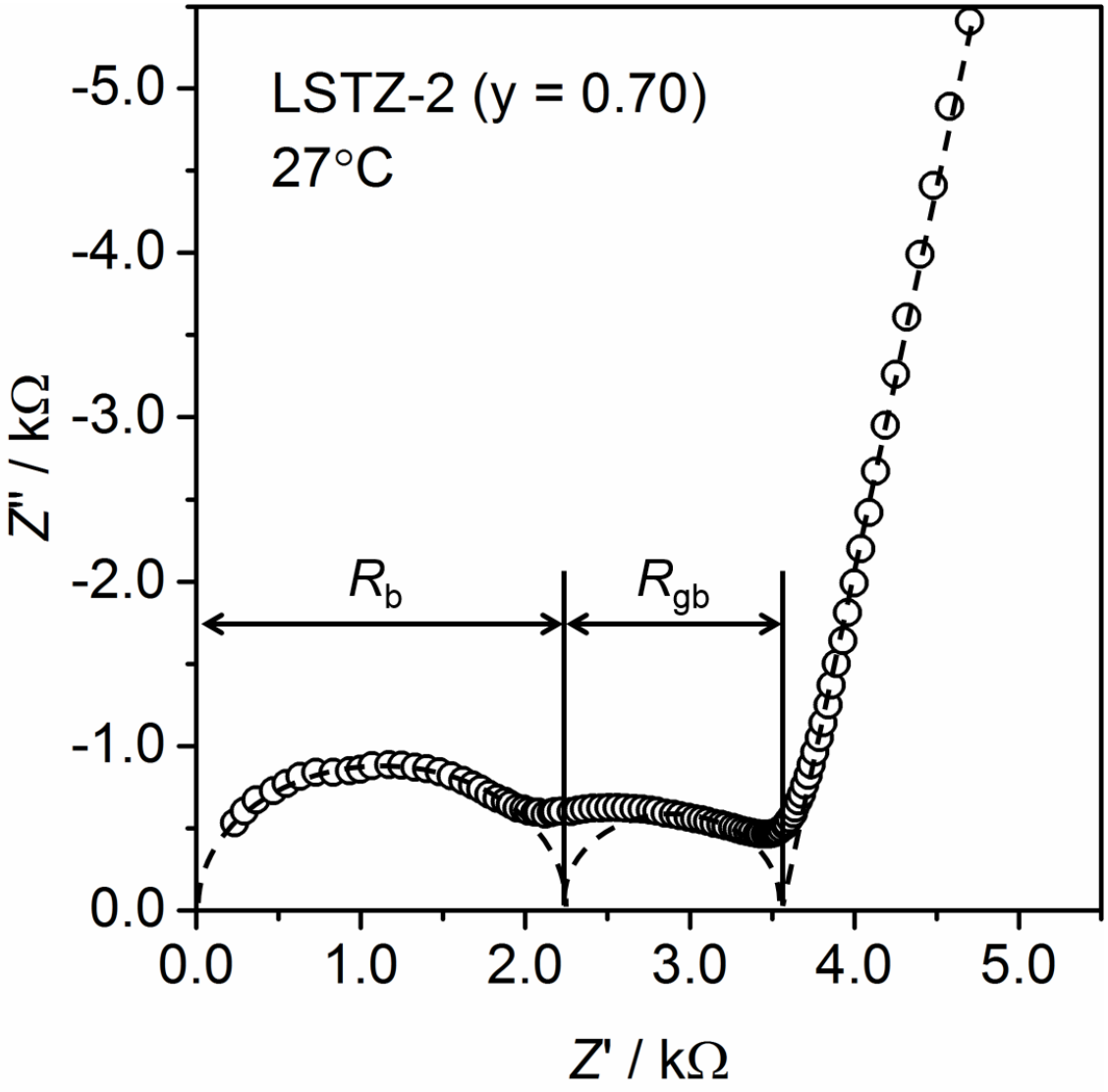

Fig. 5(b)

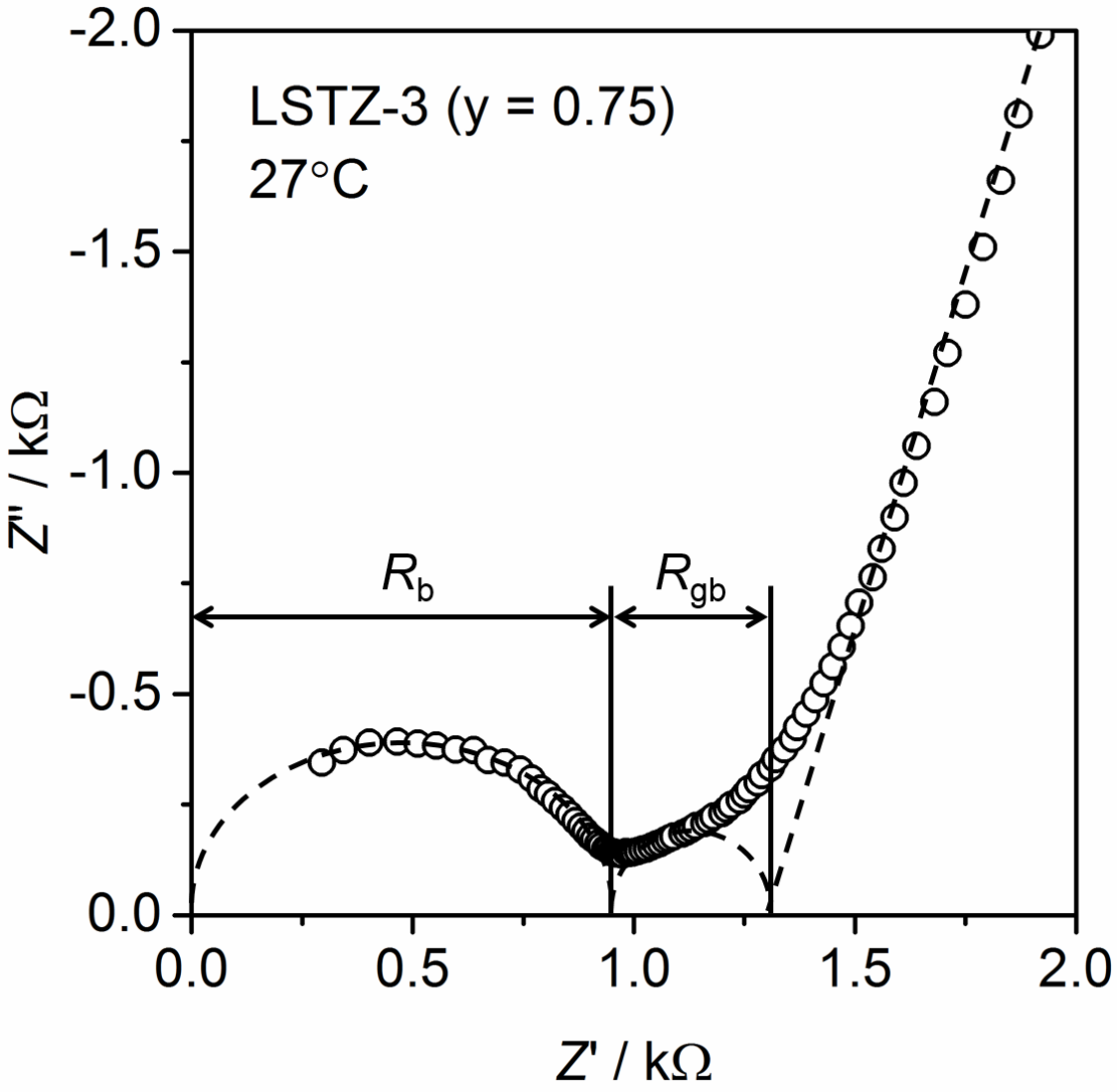

Fig. 5(c)

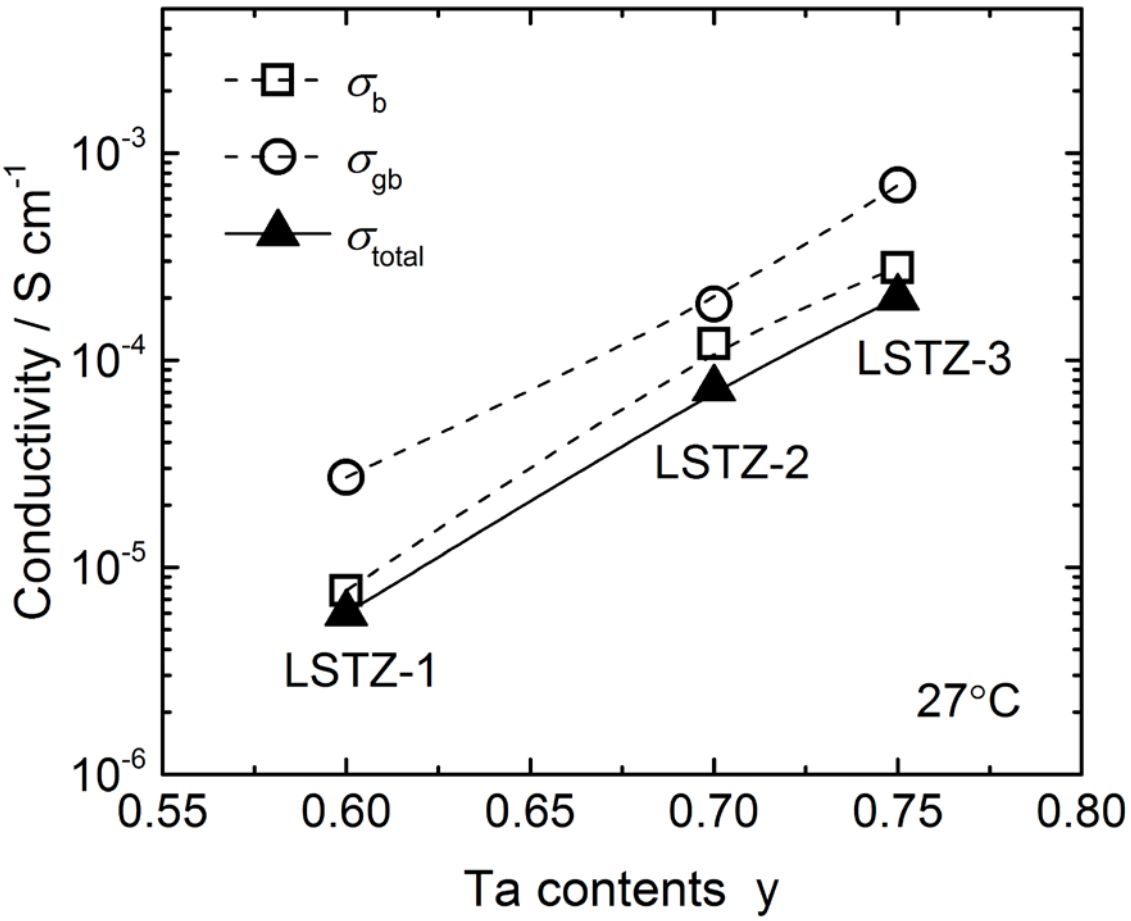
σb
σgb
σtotal
LSTZ-1
LSTZ-2
LSTZ-3
27°C
Conductivity / S cm-1
Ta contents y
10-3
10-4
10-5
10-6
0.55
0.60
0.65
0.70
0.75
0.80

Fig. 6

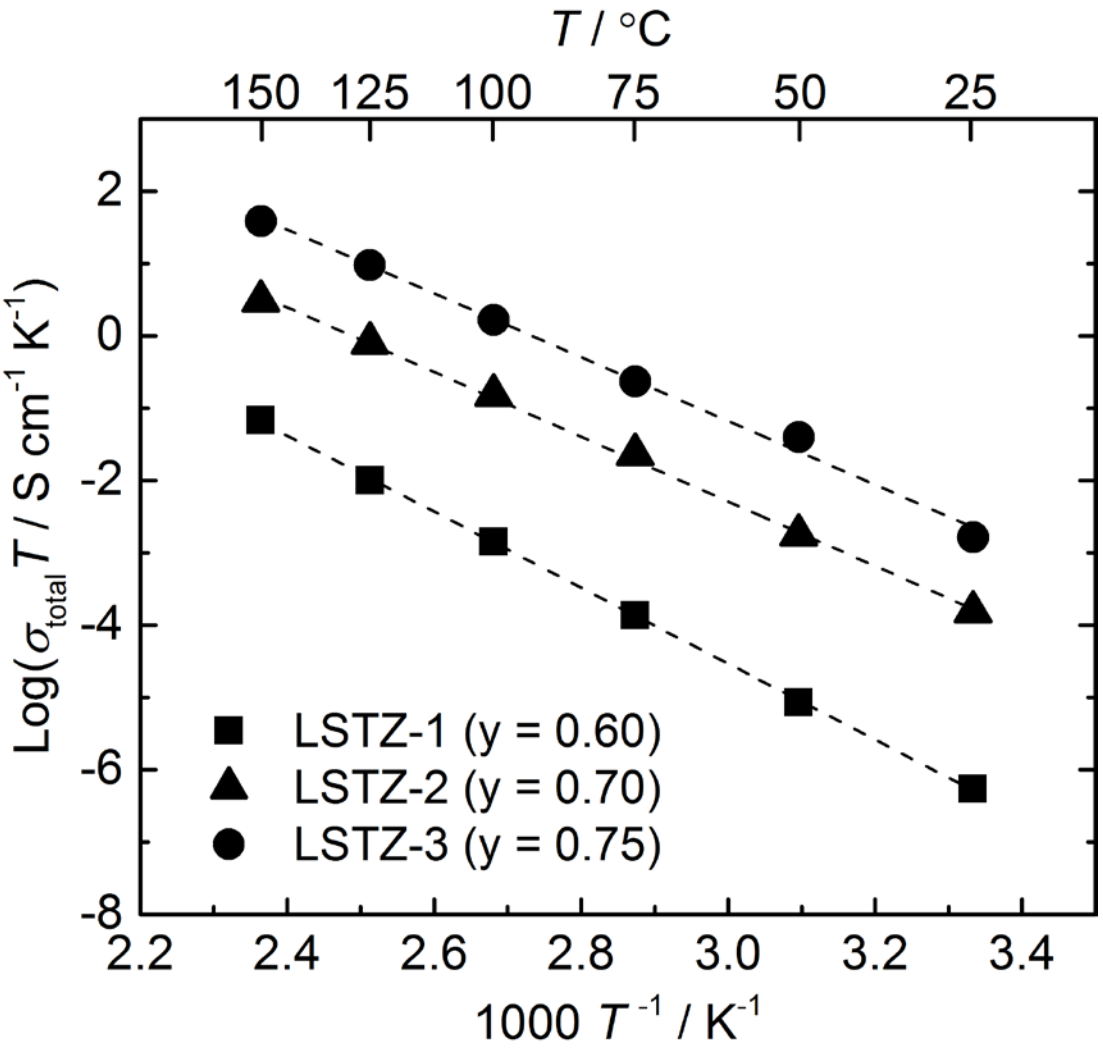
T / °C
150 125 100 75 50 25
2
0
-2
-4
-6
-8
Log(σtotal T / S cm-1 K-1)
LSTZ-1 (y = 0.60)
LSTZ-2 (y = 0.70)
LSTZ-3 (y = 0.75)
2.2 2.4 2.6 2.8 3.0 3.2 3.4
1000 T -1 / K-1

Fig. 7

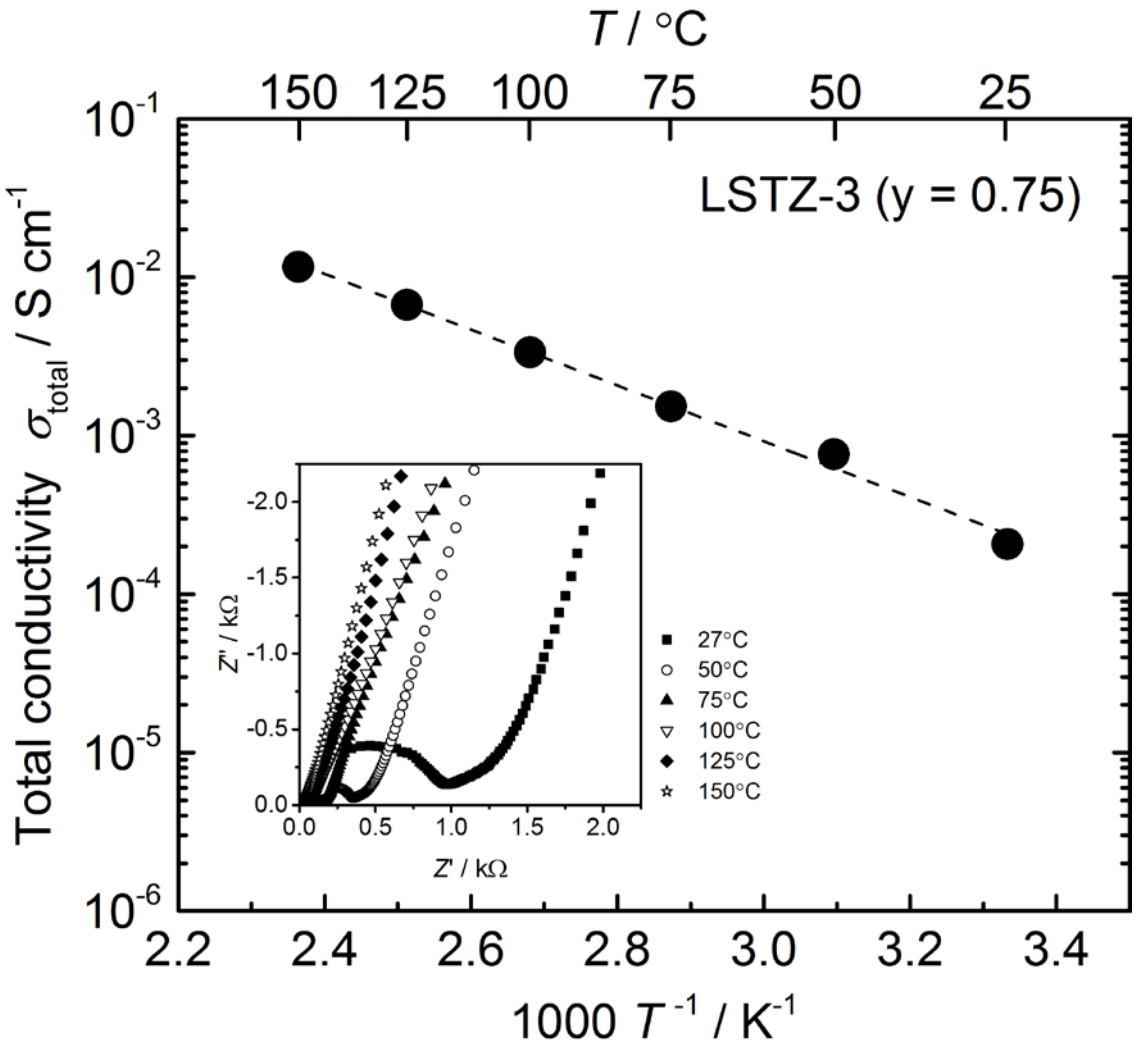
T / °C
150 125 100 75 50 25
LSTZ-3 (y = 0.75)
Total conductivity σtotal / S cm-1
10-1
10-2
10-3
10-4
10-5
10-6
2.2 2.4 2.6 2.8 3.0 3.2 3.4
1000 T-1 / K-1
Z'' / kΩ
Z' / kΩ
27°C
50°C
75°C
100°C
125°C
150°C

Fig. 8